EPR and photoluminescence spectroscopy studies on the defect structure of ZnO nanocrystals

Hülya Kaftelen,[1] Kasim Ocakoglu,[1] Ralf Thomann,[2] Suyan Tu,[3] Stefan Weber,[3] and Emre Erdem[3,*]

[1]*Advanced Technology, Research and Application Center, Mersin University, Ciftlikkoy Campus, 33343, Mersin, Turkey*

[2]*Freiburger Materialforschungszentrum (FMF), Albert-Ludwigs-Universität Freiburg, Stefan-Meier-Str. 21, 79104 Freiburg, Germany*

[3]*Institut für Physikalische Chemie, Albert-Ludwigs-Universität Freiburg, Albertstr. 21, 79104 Freiburg, Germany*

(Received 11 April 2012; revised manuscript received 19 June 2012; published 26 July 2012)

Structural and optical properties of ZnO nanoparticles can be fine tuned by a novel variant of milling performed at cryogenic temperatures. In this study intrinsic defect centers such as oxygen and zinc vacancies are characterized using electron paramagnetic resonance (EPR) and photoluminescence (PL) spectroscopy. Three different surface defects with different g factors were identified by EPR for which the spectral intensities change upon decreasing the crystal size. EPR and PL intensities revealed a linear correlation giving detailed information about optical and electronic properties of ZnO. The core-shell model established from optical emission and EPR suggests distinguished electronic states in the band gap belonging to negatively charged Zn vacancies and positively charged oxygen vacancies. This model indicates a correlation between red emission and positively charged oxygen vacancies, which lead to a possible transition from a typical n-type to a p-type ZnO semiconductor.

DOI: 10.1103/PhysRevB.86.014113 PACS number(s): 61.72.Hh

I. INTRODUCTION

Transition metal oxides with nanostructures have attracted considerable interest in many areas of chemistry, physics, and materials science. Compared to other metal oxide nanomaterials, zinc oxide (ZnO) displays novel nanostructures such as nanosprings,[1] nanobelts,[2] nanorings,[3] nanotetrapods,[4] and nanowires.[5] ZnO nanostructures can be easily distinguished by their favorable features such as the wide band gap (E_g = 3.4 eV at 300 K)[6] and their piezoelectric and pyroelectric properties.[7] For example, the energy gap in ZnO is wide enough to generate ultraviolet (UV) photons, unlike semiconductors with too narrow band gaps used in conventional lasers.[8] Because of its flexibility of forming different nanostructures, ZnO is of great interest and serves as promising material in numerous applications, particularly in piezoelectric transducers,[9] electrodes for solar cells,[10] catalyst for electronics,[11] field-effect transistors,[12] thin-film printing,[13] and transparent conductors.[14]

A number of studies have been conducted to synthesize nanocrystallite ZnO using different techniques, such as hydrothermal synthesis,[15] conventional ball-milling,[16] microwave-assisted synthesis,[17] hydrolysis/condensation,[18] and sol-gel processing.[19] Among these methods, milling in a cryogenic environment (freezer milling) allows for facile and cost-efficient fabrication. Thus, milling can be applied as a method for reducing the particle and crystallite size of materials down to the nanometer range. In addition, this technique offers advantages in controlling the microstructure of materials in terms of their crystallite size and morphology, which both strongly affect the physical, electric, electronic, and optical properties of a specific structure. All these effects have already been discussed in detail in a number of reviews.[6,20–25]

By specific mechanical and thermal treatment during high-energy ball milling, a large number of defect structures with different physical and chemical properties can be generated in the grain structure of nanostructured ZnO.[26–28] These defects allow such systems to exhibit certain desirable properties that cannot be obtained in *defect-free* crystals. In this study we demonstrate that milling at very low temperatures (77 K), as compared to room temperature high-energy ball milling,[29] accelerates the fracturing process of ZnO powders. In addition, low-temperature milling led to rapid grain refinement by suppressing recovery and recrystallization processes.

The usual approach to investigate defects is to vary their concentration by changing synthesis conditions, or by applying irradiation and/or thermal treatment, and to search for interrelated changes in measurable optical properties, such as absorption (luminescence)[20] and Raman bands.[30] Electron paramagnetic resonance (EPR), on the other hand, is a powerful technique for characterizing the magnetic properties of defect centers on an atomic scale. Correlation of EPR and optical spectroscopies hence allows one to yield a more complete insight into defect structures in general and into ZnO in particular.

Possible defect centers in ZnO are (i) zinc vacancies (V_{Zn}), (ii) zinc on interstitial sites (Zn_i), (iii) oxygen on interstitial sites (O_i), and (iv) oxygen vacancies (V_O). From the EPR point of view, the four possible centers can be distinguished as follows. (i) Zn_i as an interstitial has the electron configuration ending with $4s^2$ and is hence diamagnetic. Consequently, it is impossible to detect Zn_i defect centers by EPR. External effects (light, thermal) are required to pass an electron into the conduction band of ZnO ($Zn_i^+ + e$). A so-generated paramagnetic Zn_i^+ state can only be detected by EPR when the electronic wave functions of various Zn_i^+ centers do not overlap. (ii) Oxygen on interstitial sites (O_i) has possible electron configurations ending with $2p^4$, $2p^5$, and $2p^6$, giving O_i, O_i^-, and O_i^{2-}, respectively. The O_i^{2-} state is diamagnetic and, therefore, cannot be observed by EPR. The O_i state with the $2p^4$ configuration assumes a triplet multiplicity. The O_i^- state with the $2p^5$ electron configuration is a paramagnetic center, which can be easily detected by EPR. On the other hand, the interaction of this paramagnetic defect with other diamagnetic defects of ZnO has to be taken into account. (iii) Three possible states of oxygen vacancies can be distinguished. (1) The diamagnetic oxygen vacancy that does not trap an electron with respect to the lattice results in a doubly positively charged vacancy and can be assigned as

V_O^{2+}. It has four Zn^{2+} ions in its neighborhood, and there are no unpaired electrons left so that it is diamagnetic. (2) The vacancy of oxygen occupied by one electron is designated V_O^+. This vacancy results from reduction by one electron from the conduction band so that it is positively charged with respect to the lattice. This defect center may also be attributed to an F-center in alkali halides. (3) Finally, the vacancy-designed V_O is neutral with respect to the lattice and captures two electrons. The V_O defect center is diamagnetic if the spins of both electrons captured in the vacancy somehow compensate. If they do not, then one may expect the existence of a triplet state, which is EPR active as well but shows significantly broadened signals.

In this contribution a structural model, the so-called core-shell model of ZnO nanoparticles, is presented to offer a possible explanation for size effects in ZnO and to show that the surface shell covers the particle core with a hexagonal structure. This model has previously been applied to explain quantum-size effects for ferroelectric $PbTiO_3$ nanoparticles[31,32] prepared from a combined polymerization and pyrolysis route and to semiconductor ZnO prepared by the microwave-assisted method.[12]

II. EXPERIMENTAL

Commercial zinc oxide (ZnO) powder (Alfa Aesar 99.90%, purity) was used as starting material. The powder was milled in a magneto-ball mill (Spex 6770 Freezer mill, New Jersey, USA) for various time periods between 1 and 10 min using a liquid nitrogen (LN) medium. 5 g of ZnO powder were loaded into a polycarbonate vial and milled in a horizontal direction by magnetic shuttling of a steel impactor back and forth against two stationary end plugs. In the freezer mill experiments, the vial was immersed in LN, thereby powders do not contact the coolant. Prior to milling, samples were precooled for 10 min and afterwards were collided at a rate of 7 cps.

Milled and commercial ZnO powders were thoroughly characterized by x-ray diffraction (XRD) using a Bruker D8 Advanced Series powder diffractometer with a CuKα (0.15406 nm) radiation source employing a step size of 0.02° at a rate of 0.6°/s. Crystallite sizes and lattice strains of the milled ZnO powders were evaluated from the first three reflections of ZnO peaks for each milling time using the TOPAS 3 (Bruker AXS) software.[33] Atomic force microscopy (AFM) studies were carried out in the tapping mode using a Park System XE-100 SPM instrument. Samples for AFM investigations were prepared by drop casting a colloidal solution (a mixture of ethanol and ZnO nanoparticles) onto a mica surface. Thereafter, the samples were placed in a vacuum oven (10^{-3} Torr) at 150 °C for 1 h to evaporate the ethanol at the surface of the particles and the mica substrate.

X-band (9.33 and 9.47 GHz) and Q-band (34.2 GHz) continuous-wave EPR measurements were performed at room temperature with Bruker EMX and ESP380 spectrometers, respectively, using a rectangular TE102 (X-band) or a dielectric-ring TE011 (Q-band) resonator (both from Bruker). Calibration of the magnetic field was performed with polycrystalline DPPH (2-diphenyl-1-picrylhydrazyl) of known g factor ($g = 2.0036$). EPR spectral simulations were performed using the EasySpin toolbox from MATLAB.[34]

Photoluminescence (PL) emission spectra of the powder samples were recorded at room temperature using a Varian Cary Eclipse spectrophotometer with an excitation slit width of 20 nm and an emission slit of 10 nm. Prior to the measurements, ZnO powder samples (0.1 mol/l) were dissolved in isopropanol (i-PrOH). Absolute i-PrOH was used as the reference blank solution for the samples. The samples were excited at 325 nm, and the PL spectra were monitored as a function of the wavelength in a range between 350 nm and 800 nm.

III. RESULTS AND DISCUSSION

Control of the microstructure during milling is very important since a considerable amount of structural and microstructural defects are produced depending on the milling conditions. Note that in this study, for a collision speed of 7 cps, the milling time is the only controllable parameter during freezer milling to obtain a desired microstructure. The milling time was limited to 10 min to achieve milling efficiency and to restrict the contamination from collisions of the impactor and end plugs.

XRD patterns of the as-received (i.e., no milling) and milled ZnO powders are shown in Fig. 1. This figure also gives the crystallite sizes and lattice strain values of samples as a function of the freezer milling time. All detectable diffraction peaks in Fig. 1(a) belong to the ZnO phase [International Center for Diffraction Data (ICDD) Card no: 70-8070, Bravais lattice: primitive hexagonal, $a = b = 0.324$ nm and $c = 0.520$ nm]. No impurities or contaminations could be detected in the XRD analyses of ZnO powders after milling for different durations. Sharp diffraction peaks of ZnO were observed for the as-received powders, whereas a considerable broadening of peaks concomitant with a decrease in intensity was noticed with increasing milling time [Fig. 1(b)]. This indicates crystallite size refinement of ZnO as well as the accumulation of internal strain [Fig. 1(c)].

During freezer milling, the repeated action of the steel rod against two stationary end plugs leads to squeezing of powders between them. This impact induces a series of repeated fragmentations. Thus, powders are subjected to extensive and repeated plastic deformation. This impact also introduces strain into the powder; as a result, the crystallites rupture down to the nanometer range. The average crystallite sizes of the ZnO phase in both the as-received and the milled powders were obtained from the XRD data (Fig. 1) using a convolution profile fitting procedure. This profile fitting is normally associated with microstructure analysis where the sample contribution needs to be separated from the instrument contribution in an observed profile.[36] The profile-fitting function applies the Debye-Scherrer formula[37] to estimate the crystallite size based on individual peak widths. Figure 1(c) represents the variation of the average crystallite sizes and lattice strains of ZnO particles as a function of milling duration. The average crystallite size of ZnO decreases from 221 nm to about 89 nm, whereas the lattice strain increases up to 0.378% for the prolonged milling time (10 min). Scanning and transmission electron micrograph (SEM and TEM, respectively) results are consistent with the XRD data in terms of obtained crystal

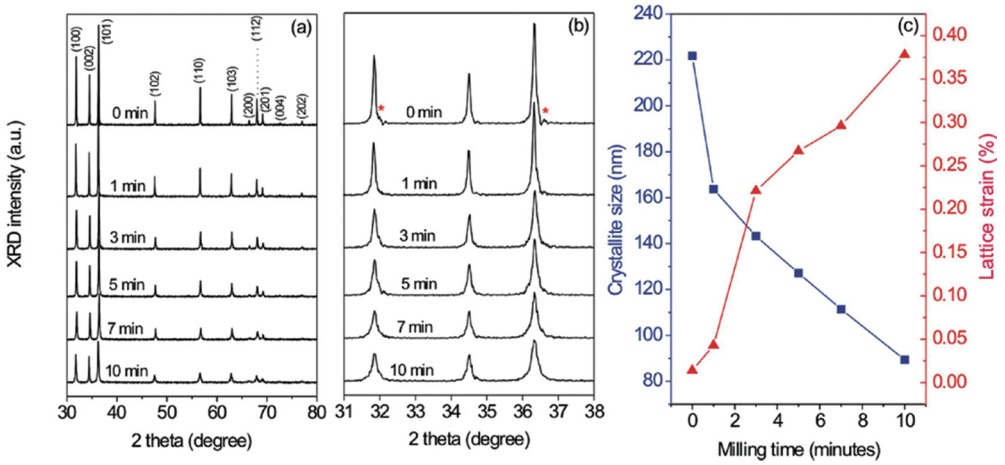

FIG. 1. (Color online) XRD patterns of ZnO powders for various milling times for 2θ in the range of (a) 30–80° and (b) 31–38°, and (c) average crystallite sizes and lattice strains of ZnO particles as a function of milling time. Asterisks (*) in (b) indicate residual Kα_2.[35]

sizes (see supplementary material[38] for representative SEM and TEM results on the ZnO sample that was milled for 7 min).

AFM investigations were conducted to reveal the morphological features (particle shape, size, and surface morphology) of ZnO nanoparticles. Figures 2(a) and 2(b) show representative noncontact AFM images of ZnO particles generated by freezer milling for 10 min. Figure 2(c) gives the line-scan profile analysis results taken from the data in Fig. 2(b).

This image also shows the presence of uniformly distributed ZnO nanoparticles with high spatial density. Based on the line-scan profile analysis result in Fig. 2(c), the typical size for ZnO particles is in the 119–171 nm range, and the average particle size calculated from the image analysis is (144 ± 18) nm. Note that the average particle size with its standard deviation was calculated by measuring the size of 10 different particles using a total of five AFM images from various regions of the ZnO nanopowders (milled for 10 min). Our XRD and AFM results are consistent with a core-shell structure:

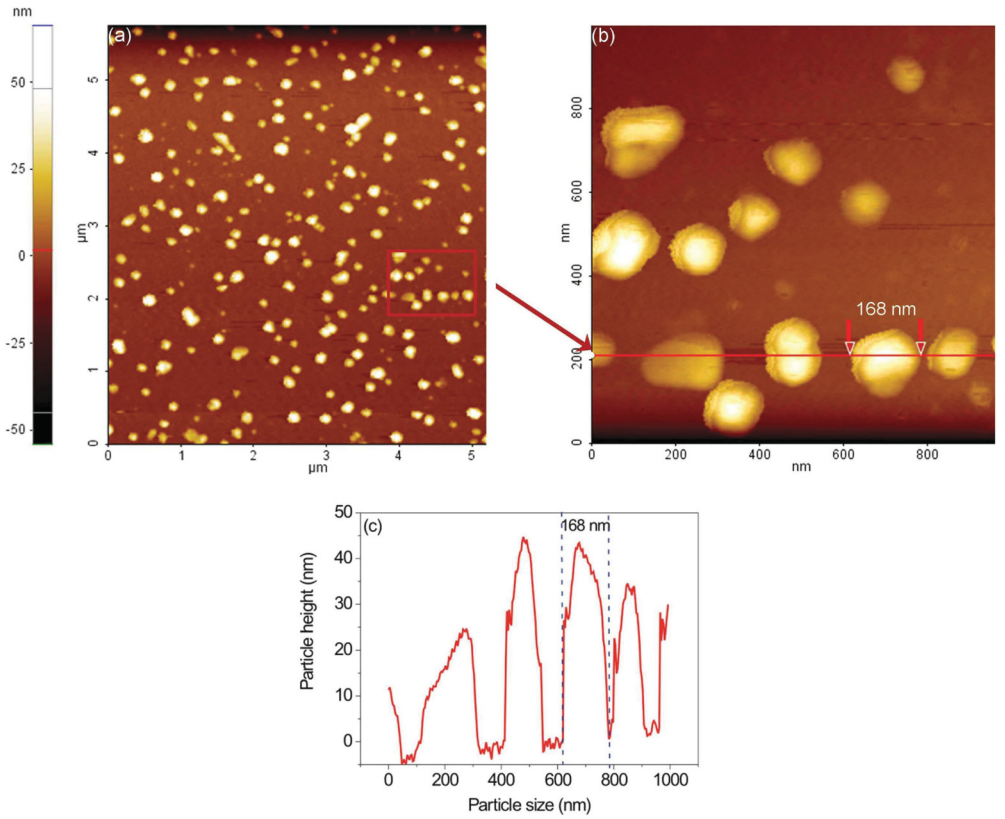

FIG. 2. (Color online) (a) AFM image of ZnO nanocrystallite particles obtained by 10 min of freezer milling; (b) an expanded image of the red region shown in (a); (c) line-scan profile analysis taken along the trace shown in (b).

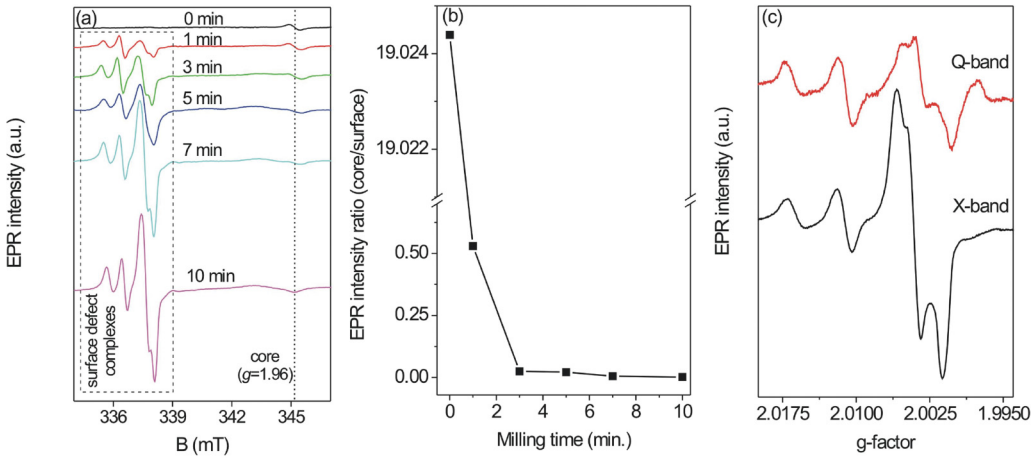

FIG. 3. (Color online) (a) X-band (9.33 GHz) EPR measurements at room temperature for 0–10 min freezer-milled ZnO samples; (b) ratios of core and surface defect centers deduced from X-band EPR intensity as a function of the milling time; and (c) comparison of X- and Q-band EPR signals on a common g-factor scale.

AFM images yield the geometrical size of the entire particles (core + shell + agglomerates), and the XRD analyses reveal only the crystallite size (core).

In order to further investigate intrinsic defect centers generated during freezer milling, X-band and Q-band EPR measurements were carried out on ZnO samples as a function of particle size. Figure 3(a) shows the room temperature X-band EPR signal of the as-received (no milling) ZnO sample and also those of freezer-milled ZnO samples for different milling durations (1–10 min). Contaminations of the samples from either metal ions, such as Mn^{2+}, Fe^{3+}, or Cr^{3+} (which can in principle be easily detected by EPR even at extremely low concentrations), or from nitrogen (EPR-active state: N^0), are not observed and can therefore be excluded. Preliminary EPR investigations of samples that were milled for durations longer than 10 min did not reveal further spectral changes (data not shown).

Inspection of Fig. 3(a) reveals that, except for the as-received powder, all freezer-milled ZnO samples exhibit the same types of paramagnetic defect centers. The unmilled ZnO sample shows only one single EPR line at $g = 1.960$ [Fig. 3(a)] that has already been reported in the literature.[39–44] However, the origin of this intrinsic defect signal has been controversially discussed; assignments to shallow donors, singly ionized oxygen vacancies, Zn vacancies, or oxygen and zinc interstitials have been put forward. This controversy can be at least partially resolved by assigning the signal at $g = 1.960$ to a core signal in the framework of the core-shell model.[45] The line shape of this core signal changes with increasing milling time, thus indicating strong size effects due to the confinement of electrons in the core.[45]

Surface defects (on the shell) were observed by EPR for the milled samples (1–10 min of freezer milling) and are depicted in Fig. 3. The resonances for X-band EPR measurements at room temperature are highlighted with a dashed rectangle in Fig. 3(a). The intensities of EPR signals arising from surface defects (shell) significantly increase with increasing freezer milling time. Interestingly, for the case of bulk ZnO, the EPR signal at around $g \sim 2.00$ has been controversially discussed in the literature: assignment to a singly ionized Zn vacancy,[46,47] or to an unpaired electron trapped on an oxygen vacancy site,[40,48,49] i.e., an F^+ center, have been put forward.[50] The former assignment was based on the resolved hyperfine interaction with the four neighboring Zn nuclei, which, however, was only observed when ZnO was irradiated.[51] This observation is also consistent with results from density functional theory (DFT) calculations,[52] which indicate that a certain excitation is required to generate the paramagnetic +1 state. On the other hand, the oxygen vacancies at the ZnO surfaces[53] are stable and could trap electrons to form paramagnetic centers (F^+ centers). This could also account for the stable EPR signal at $g \sim 2.00$.

The core and shell signal intensity ratios obtained from an analysis of the EPR spectra are presented in Fig. 3(b). A strong reduction of the core intensity after just 1 min of milling by a factor of nearly 40 is observed. The shell thickness for ZnO samples prepared by a microwave-assisted route has already been determined as 1 nm.[12]

Q-band EPR was employed to take advantage of the higher sensitivity of EPR at higher frequencies and to attain better spectral resolution of defect centers in ZnO samples. A comparison of X-band and Q-band EPR signals calibrated to a common g-scale is shown in Fig. 3(c). The g factors refer to the ZnO sample milled for 1 min. Both X- and Q-band spectra reveal virtually the same spectral features with respect to the g factor [Fig. 3(b)].

To determine the concentrations and relative EPR intensity ratios of various defect centers, accurate simulations are required. By the aid of spectral simulations we clearly resolve and identify three magnetically inequivalent EPR signals that belong to three different defect centers, in the following named D1, D2, and D3. Their origin will be discussed below. Figure 4 shows a comparison of experimental and simulated EPR spectra for the ZnO sample that was milled for 10 min. The contributions of D1 and D2 to the overall EPR spectrum are clearly anisotropic whereas that of D3 is isotropic (see parameters listed in Table I). The relative contributions of D1, D2, and D3 are 1.0097, 0.1401, and 0.0489, respectively

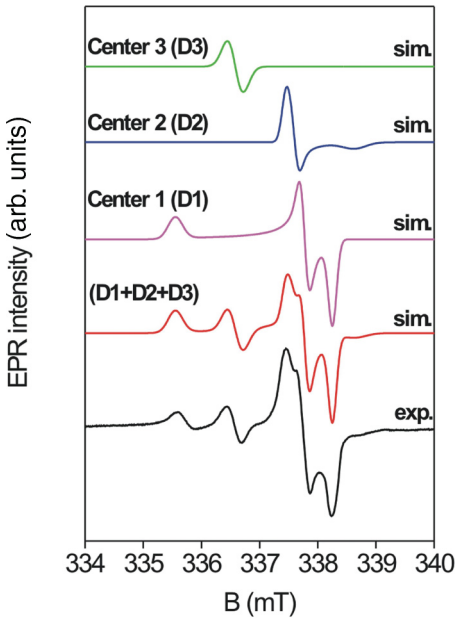

FIG. 4. (Color online) Room temperature X-band (9.47 GHz) EPR spectrum for the 10 min freezer-milled ZnO sample (black curve) and its overall spectral simulation (red/dark gray curve). The green (light gray), blue (medium gray), and violet (gray) curves show spectral contributions of D3, D2, and D1, respectively. The overall EPR spectrum (intensity I_{total}) is built up from the contributions of D1, D2, and D3 as follows: $I_{\text{total}} = 1.0097$, $I_{\text{D1}} + 0.1401$, $I_{\text{D2}} + 0.0489$ I_{D3}.

(normalized: D1 + 7.2D2 + 20.6D3). All defect centers have $S = 1/2$; no resolved hyperfine coupling or zero-field splitting was observed. Hence, only the contribution arising from the Zeeman interaction has to be considered in the spin Hamiltonian.

The thermal stability and atmospheric reactivity of all defect centers, D1, D2, and D3, were also investigated by EPR under certain atmospheres (vacuum, argon, and nitrogen) at an annealing temperature of 240 °C. Additionally, the microwave power saturation behavior of the defect centers was investigated. (Details on stability, reactivity and saturation measurements can be found in the supplementary material.[38])

To complement our EPR investigations and to gain more insight into the electronic structure, PL measurements were carried out. PL data taken from both the UV and the visible spectral region can be found in the literature.[6,54] However, the origin and the mechanism underlying the luminescence centers are not well understood[6,26,54]; occasionally, assignments have been put forward without compelling experimental evidence. Thus, the nature of the green luminescence (GL),[42,44,55,56] orange-red luminescence (ORL),[57] and yellow luminescence (YL)[58] bands remain controversial. In undoped ZnO, the GL peak usually dominates the defect-related part of the PL spectrum[54] and was attributed to oxygen vacancies. Others proposed that GL in ZnO originates from metal impurities[42] or from a transition between a singly charged oxygen vacancy and a photo-excited hole.[44] YL and ORL bands are only detectable under certain preparation conditions,[54] such as Li doping and annealing at high temperatures under air, respectively. Both emissions were attributed to oxygen interstitials.[54] Also, the simultaneous existence of blue and yellow emissions in ZnO was explained by two different processes. The first process involves the recombination of a shallow-trapped electron with a deep trapped hole due to the presence of oxygen vacancies, and the second process involves the recombination of a shallow-trapped electron with a shallow-trapped hole due to the presence of the amine ligand at the surface.[59] Recent analyses of electroluminescence data on ZnO confirmed that the red emissions in the range from 620 to 690 nm arise from oxygen interstitials and those in the range from 690 to 750 nm from oxygen vacancies.[60] We believe that one can resolve such controversy by combining the results from EPR and PL spectroscopies.

Freezer milling introduces metastable electronic states in the band gap, and these defects are expected to influence optical emission. Figure 5(a) shows the PL emission spectra of both unmilled and milled ZnO samples upon excitation at 325 nm. The emission spectra of all samples display one peak in the UV region at 388 nm, which is a near band-edge emission.[61] It is usually considered a characteristic emission of ZnO and is attributed to band-edge emission or donor-band excitation.[16] However, in many PL reports, this characteristic peak in the UV region does not appear;[16,44] for example, it was suppressed in ZnO nanowires, which were produced by high-energy ball milling and annealing methods.[16] We suggest, opposite to some reports in the literature, that the presence of the emission at 388 nm is likely due to differences in powder preparation methods, i.e., room temperature high-energy ball milling as compared to freezer milling. By the latter method, ZnO particles become more brittle and hence are more likely to crack into nanosize. Furthermore, since defect generation is temperature dependent, annihilation of defects might occur during temperature rises in the conventional ball milling method, thus leading to altered PL spectra.

On the other hand, we observed a very intense broad emission at 470 nm [see Fig. 5(a)]. This signal disappears when the milling time exceeds 1 min. Emissions in the visible range are generally considered to be induced by defects, the concentration of which increases with milling time. For example, beyond the 3 min of freezer milling, a sharp signal emerges in the red range at around 655 nm.[26] Previously[62–64] this emission was attributed to transitions between neutral and singly ionized oxygen vacancies. According to our core-shell description, core defects dominate the optical properties of

TABLE I. Room temperature X-band EPR parameters obtained from a spectral simulation for the 10-min freezer-milled ZnO sample.

Defect center (at the surface)	g factor	FWHM linewidth [mT]
D1	$g_x = 2.001(1)$ $g_y = 2.004(1)$ $g_z = 2.017(1)$	0.21
D2	$g_x = 2.006(1)$ $g_y = 2.004(1)$ $g_z = 1.998(1)$	0.24
D3	$g_{\text{iso}} = 2.011(1)$	0.37

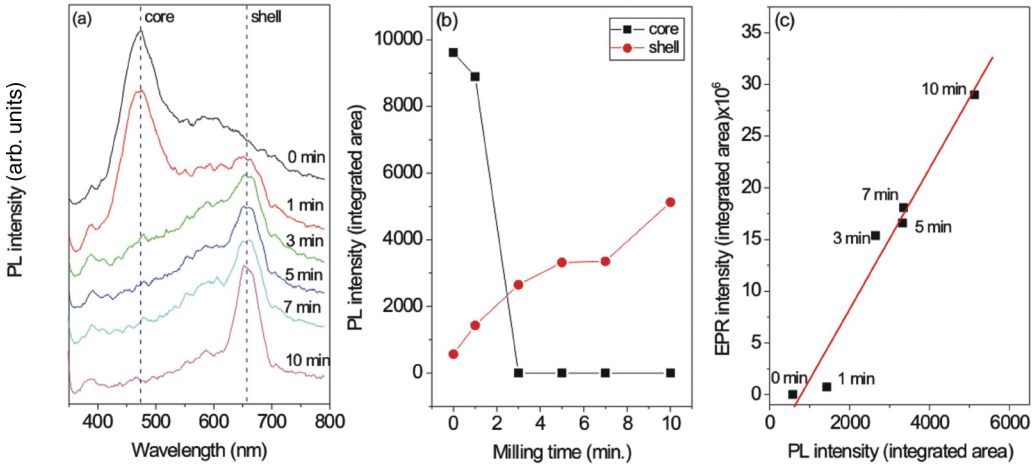

FIG. 5. (Color online) (a) PL spectra recorded at room temperature, (b) integrated area of core and shell signals from PL spectra (for details, see text), and (c) linear relation of EPR spectral intensity and PL signal intensity (at 655 nm) for the surface defects (shell).

ZnO in the bulk. Thus, bulk ZnO emits energetically higher blue light than nanosized particles that emit red light. The situation is reversed when reducing the particle size by increasing the milling time. In this case, as is seen in Fig. 5(b), surface defects become dominant, and the intensity of the red-light emission at 655 nm increases drastically.

A similar trend is observed for the intensity of the EPR surface defect signals [Fig. 3(a)], and indeed, the PL intensity at 655 nm can be linearly correlated with the EPR signal intensities of surface defects at the various milling times [Fig. 5(c)]. From this linearity we conclude that singly ionized oxygen vacancies (V_O^+) are the origin of the red emission in the PL data. This suggestion is consistent with recent electroluminescence measurements.[60]

To establish a relation between the EPR and PL measurements, a model for nanocrystalline ZnO is shown schematically in Fig. 6. By increasing the strain during milling, the interior core becomes negatively charged due to an increase of V_{Zn}^- defects. V_{Zn}^- has spin quantum number $S = 1/2$, and therefore it reveals a typical single EPR line at $g \sim 1.96$. In principle, one could also attribute the same signal of bulk ZnO to the oxygen vacancies which are positively charged. However, according to our EPR and PL results, the core-shell model supports the negative charging of core and positive charging of the shell. This is mainly due to the decrease of the EPR signal at $g \sim 1.96$ upon decreasing the crystal (core) size. Clearly, more oxygen vacancies are formed on the surface than in the core. The oxygen vacancies formed on the surface can trap either one (V_O^+) or two electrons (V_O) upon irradiation of the crystal with high-energy electrons or neutrons.

As seen in Figs. 3 and 4, we observe an overlap of three different EPR signals (D1, D2, and D3) belonging to oxygen vacancies in the shell. Estimated from the relative intensity ratio of these defects (see Fig. 3), most show low symmetry, thus leading to a rhombic EPR signal (D1); whereas the others, however, occurring much less frequently, have higher symmetry, thus producing nearly axial symmetric (D2) and isotropic (D3) EPR signal contributions. Although conclusive evidence still needs to be presented, one could, in a very

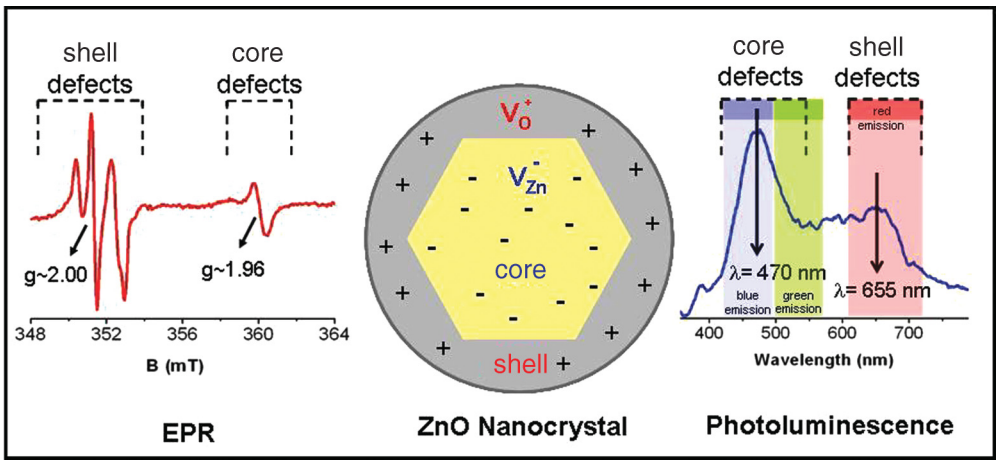

FIG. 6. (Color online) Schematic illustration of a ZnO nanocrystal, obtained from freezer milling. It consists of a negatively charged interior core and a positively charged outer shell. The EPR and PL spectra are given for the 1 min milled sample where we clearly observe core and shell defects simultaneously.

simple picture, tentatively assign D1 to defects that are in close proximity to the surface of the nanoparticle where one would expect that they be generated at rather high concentration. The D2 defects, on the other hand, could be localized very near the core. Their symmetry, roughly axial symmetric, reports on the core structure, which is strongly influenced by the Zn vacancies that are known to be surrounded by four oxygen lattice ions in a tetrahedron, which is trigonally distorted along the c axis.[51] Finally, the D3 defects could be localized in between the core/shell boundary and the nanoparticle surface. Their signal, being isotropic with rather large inhomogeneous line width, reports on the featureless interphase that provides a surrounding that is effectively isotropic in symmetry. Our attempts to characterize the stability/reactivity of the defects D1, D2, and D3 (see supplementary material[38]) corroborate our tentative assignment with the D1 and D3 defects being surface exposed. Hence they are more susceptible towards changes in the surroundings and D2 near the core, thus showing rather good resistibility towards thermal treatment. But again, this assignment should be considered preliminary. Clearly, further studies need to be performed to corroborate these notions. In any case, our data provide strong evidence for three *magnetically inequivalent* nanocrystalline sites.

Our observations lead to a possible transition from typical n-type ZnO to p-type ZnO semiconduction when going from bulk to nano size. On the other hand, we present evidence for a core-shell structure from our optical emission spectra which shows that core defects (V_{Zn}^{-}) emit mainly blue (2.63 eV) and partly green (2.21–2.48 eV) light whereas shell defects emit red (1.89 eV) light; the lower photon energy excites surface defects rather than core defects, because core defects are shallow acceptors and surface defects are deep donors.

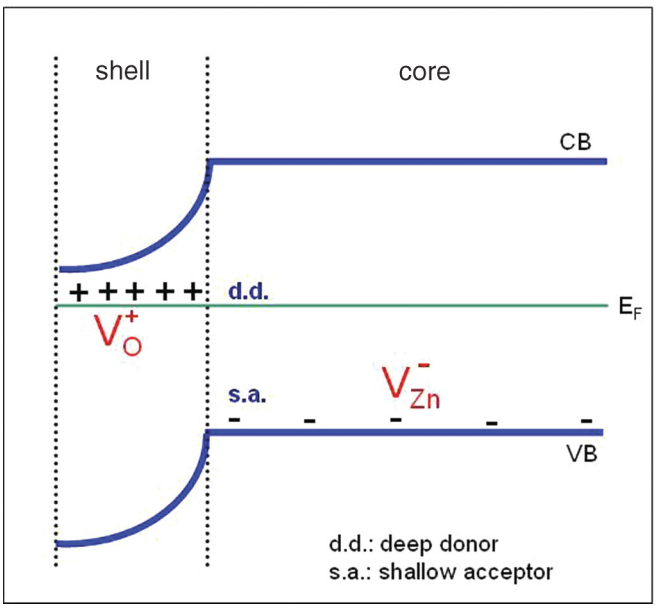

FIG. 7. (Color online) Sketch of the band gap as a function of the defect structure in core-shell structured nano-sized ZnO synthesized by the freezer milling method. It shows that the oxygen vacancies at the surface act as deep donors and the Zn vacancies in the core act as shallow acceptors.

Figure 7 presents a schematic diagram of our defect model. The core is dominated primarily by shallow acceptors whereas at the shell deep donors prevail. As a consequence, the development of p-type ZnO is favorable for sufficiently small particle sizes. The core-shell model suggests the negative charge of the core and the positive charge of the shell. This is supported not only by the decrease in EPR intensity of the signal at $g \sim 1.96$ but also the increasing amount of red-light emission in the PL data when decreasing the crystal (core) size. Evidently, the concentration of positively charged oxygen vacancies increases drastically in the shell rather than in the core, and conversely, more negatively charged Zn vacancies are formed in the core than at the surface.

IV. CONCLUSIONS

The present study provides detailed information on the structural and optical properties of ZnO powders as a function of freezer milling time. Using our facile freezer milling method, highly uniform and homogeneously dispersed ZnO nanoparticles having nanocrystallite sizes below 100 nm were obtained after 10 min of milling. Therefore, it can be suggested that the desired crystallite size is controllable only with the milling time (for a constant collision speed) by using the freezer milling method. To understand the appearance and behavior of intrinsic defect centers in ZnO powders that were milled for different times, advanced EPR and PL studies were combined. A linear correlation has been found for the signal intensities arising from the surface. EPR (yielding information on the defect surroundings) and PL (yielding information on excitation energies) results also confirm the core-shell model of ZnO, where the core is still hexagonal and contains negatively charged Zn vacancies and the shell is a medium containing high concentrations of defect complexes, in particular positively charged oxygen vacancies, thus resulting in a selective behavior of defect centers towards different excitation energies (optically vs microwave). This, in principle, allows the material to become a p-type semiconductor.

For technological applications in semiconductor research, further improvement can be achieved by developing novel strategies to adjust the parameters of core-shell nanomaterials and to control defect concentrations. This result will push the limits of p-type ZnO production and might be helpful for technological applications in multidisciplinary fields, such as in electronics and biomedicine.

ACKNOWLEDGMENTS

This research has been financially supported by the Deutsche Forschungsgemeinschaft, DFG (Grant No. Er 662/1-1) and the Scientific and Technological Research Council of Turkey, TUBITAK (Grant No. 110M803) in the framework of the European Science Foundation (ESF-EUROCORES-EuroSolarFuels-10-FP-006). The authors would like to thank G. Yildiz from Yildiz Analiz Co. (Ankara, Turkey) for freezer milling experiments, MSc. S. Sönmez (Mersin University) for the PL measurements, T. Berthold (University of Freiburg) for EPR measurements, and R. Böttcher (University of Leipzig), R.-A. Eichel (KIT), P. Jakes (KIT), and A. Eisenmeier (University of Freiburg) for valuable discussions.

*Corresponding author: emre.erdem@physchem.uni-freiburg.de

[1] X. Y. Kong and Z. L. Wang, Nano Lett. **3**, 1625 (2003).

[2] Z. W. Pan, Z. R. Dai, and Z. L. Wang, Science **291**, 1947 (2001).

[3] X. Y. Kong, Y. Ding, R. Yang, and Z. L. Wang, Science **303**, 1348 (2004).

[4] A. K. Srivastava, M. Deepa, K. N. Sood, E. Erdem, and R.-A. Eichel, Adv. Mater. Lett. **2**, 142 (2011).

[5] X. Wu, P. Jiang, Y. Ding, W. Cai, S.-S. Xie, and Z. L. Wang, Adv. Mater. **19**, 2319 (2007).

[6] U. Ozgur, Y. I. Alivov, C. Liu, A. Teke, M. A. Reshchikov, S. Dogan, V. Avrutin, S. J. Cho, and H. Morkoc, J. Appl. Phys. **98**, 041301 (2005).

[7] Z. L. Wang, J. Phys.: Condens. Matter **16**, R829 (2004).

[8] F. Gao, N. Chino, S. P. Naik, Y. Sasaki, and T. Okubo, Mater. Lett. **61**, 3179 (2007).

[9] D. C. Look, Mater. Sci. Eng. B **80**, 383 (2001).

[10] A. B. F. Martinson, J. W. Elam, J. T. Hupp, and M. J. Pellin, Nano Lett. **7**, 2183 (2007).

[11] S. Couet, T. Seldrum, C. Moisson, D. Turover, R. Sporken, and J. Dumont, Appl. Phys. A **88**, 111 (2007).

[12] J. J. Schneider, R. C. Hoffmann, J. Engstler, A. Klyszcz, E. Erdem, P. Jakes, R. A. Eichel, L. Pitta-Bauermann, and J. Bill, Chem. Mat. **22**, 2203 (2010).

[13] J. J. Schneider, R. C. Hoffmann, J. Engstler, S. Dilfer, A. Klyszcz, E. Erdem, P. Jakes, and R. A. Eichel, J. Mater. Chem. **19**, 1449 (2009).

[14] Z. A. Wang, J. B. Chu, H. B. Zhu, Z. Sun, Y. W. Chen, and S. M. Huang, Solid State Electron. **53**, 1149 (2009).

[15] W. J. Li, E. W. Shi, Y. Q. Zheng, and Z. W. Yin, J. Mater. Sci. Lett. **20**, 1381 (2001).

[16] A. M. Glushenkov, H. Z. Zhang, J. Zou, G. Q. Lu, and Y. Chen, Nanotechnology **18**, 175604 (2007).

[17] N. Takahashi, Mater. Lett. **62**, 1652 (2008).

[18] A. W. Cohn, K. R. Kittilstved, and D. R. Gamelin, J. Am. Chem. Soc. **134**, 7937 (2012).

[19] D. W. Bahnemann, C. Kormann, and M. R. Hoffmann, J. Phys. Chem. **91**, 3789 (1987).

[20] A. B. Djurisic and Y. H. Leung, Small **2**, 944 (2006).

[21] G. Hodes, Adv. Mater. **19**, 639 (2007).

[22] V. Ischenko, S. Polarz, D. Grote, V. Stavarache, K. Fink, and M. Driess, Adv. Funct. Mater. **15**, 1945 (2005).

[23] A. Janotti and C. G. V. de Walle, Phys. Rev. B **76**, 165202 (2007).

[24] M. D. McCluskey and S. J. Jokela, J. Appl. Phys. **106**, 071101 (2009).

[25] K. M. Whitaker, S. T. Ochsenbein, A. L. Smith, D. C. Echodu, B. H. Robinson, and D. R. Gamelin, J. Phys. Chem. C **114**, 14467 (2012).

[26] A. B. Djurisic, Y. H. Leung, K. H. Tam, L. Ding, W. K. Ge, H. Y. Chen, and S. Gwo, Appl. Phys. Lett. **88**, 103107 (2006).

[27] M. Kakazey, M. Vlasova, M. Dominguez-Patino, and J. Munguia-Diaz, Solid State Commun. **145**, 122 (2008).

[28] L. Schmidt-Mende and J. L. MacManus-Driscoll, Materials Today **10**, 40 (2007).

[29] S. K. S. Parashar, B. S. Murty, S. Repp, S. Weber, and E. Erdem, J. Appl. Phys. **111**, 113712 (2012).

[30] J. M. Calleja and M. Cardona, Phys. Rev. B **16**, 3753 (1977).

[31] E. Erdem, K. Kiraz, M. Somer, and R.-A. Eichel, J. Eur. Ceram. Soc. **30**, 289 (2010).

[32] E. Erdem, H. C. Semmelhack, R. Bottcher, H. Rumpf, J. Banys, A. Matthes, H. J. Glasel, D. Hirsch, and E. Hartmann, J. Phys.: Condens. Matter **18**, 3861 (2006).

[33] A. A. Kern and A. A. Coelho, (www.brukeraxs.com, 2006).

[34] S. Stoll and A. Schweiger, J. Magn. Reson. **178**, 42 (2006).

[35] D. Louer, J. P. Auffredic, J. I. Langford, D. Ciosmak, and J. C. Niepce, J. Appl. Cryst. **16**, 183 (1983).

[36] R. W. Cheary and A. Coelho, J. Appl. Cryst. **25**, 109 (1992).

[37] B. D. Cullity and R. D. Stock, *Elements of X-ray Diffraction* (Prentice-Hall Inc., Massachusetts, 2001).

[38] See Supplemental Material at http://link.aps.org/supplemental/10.1103/PhysRevB.86.014113 for detailed morphology investigations of core-shell structure by SEM and TEM. Reactivity and the stability of the D1, D2, and D3 defect centers can be also found in this supplementary material. Microwave saturation dependency and atmospheric (air, vacuum, nitrogen, and argon) activity of the samples have been investigated by continuous-wave EPR.

[39] K. M. Sancier, J. Phys. Chem. **76**, 2527 (1972).

[40] B. L. Yu, C. S. Zhu, F. X. Gan, and Y. B. Huang, Mater. Lett. **33**, 247 (1998).

[41] S. M. Evans, N. C. Giles, L. E. Halliburton, and L. A. Kappers, J. Appl. Phys. **103**, 043710 (2008).

[42] N. Y. Garces, L. Wang, L. Bai, N. C. Giles, L. E. Halliburton, and G. Cantwell, Appl. Phys. Lett. **81**, 622 (2002).

[43] Y. Hu and H. J. Chen, J. Nanopart. Res. **10**, 401 (2008).

[44] K. Vanheusden, W. L. Warren, C. H. Seager, D. R. Tallant, J. A. Voigt, and B. E. Gnade, J. Appl. Phys. **79**, 7983 (1996).

[45] P. Jakes and E. Erdem, Phys. Status Solidi-RRL **5**, 56 (2011).

[46] D. Galland and A. Herve, Phys. Lett. A **33**, 1 (1970).

[47] A. L. Taylor, G. Filipovi, and Gk. Lindeber, Solid State Commun. **8**, 1359 (1970).

[48] L. Q. Jing, Z. L. Xu, J. Shang, X. J. Sun, W. M. Cai, and H. C. Guo, Mater. Sci. Eng. A **332**, 356 (2002).

[49] L. Y. Zhang, L. W. Yin, C. X. Wang, N. Lun, Y. X. Qi, and D. Xiang, J. Phys. Chem. C **114**, 9651 (2010).

[50] N. G. Kakazey, T. V. Sreckovic, and M. M. Ristic, J. Mater. Sci. **32**, 4619 (1997).

[51] A. Poppl and G. Volkel, Phys. Status Solidi A **125**, 571 (1991).

[52] A. Janotti and C. G. Van de Walle, Appl. Phys. Lett. **87**, 122102 (2005).

[53] M. Kakazey, M. Vlasova, M. Dominguez-Patino, G. Dominguez-Patino, T. Sreckovic, and N. Nikolic, Sci. Sintering **36**, 65 (2004).

[54] A. Janotti and C. G. Van de Walle, Rep. Prog. Phys. **72**, 126501 (2009).

[55] Y. W. Heo, D. P. Norton, and S. J. Pearton, J. Appl. Phys. **98**, 073502 (2005).

[56] Z. G. Wang, X. T. Zu, S. Zhu, and L. M. Wang, Physica E **35**, 199 (2006).

[57] G. H. Du, Y. Q. Yang, T. B. Li, and B. S. Xu, J. Mater. Sci. **45**, 1464 (2010).

[58] M. A. Reshchikov, J. Q. Xie, B. Hertog, and A. Osinsky, J. Appl. Phys. **103**, 103514 (2008).

[59]W. S. Khan, C. Cao, Z. Chen, and G. Nabi, Mater. Chem. Phys. **124**, 493 (2010).
[60]N. H. Alvi, K. ul Hasan, O. Nur, and M. Willander, Nanoscale Res. Lett. **6**, 7 (2011).
[61]R. M. Nyffenegger, B. Craft, M. Shaaban, S. Gorer, G. Erley, and R. M. Penner, Chem. Mater. **10**, 1120 (1998).
[62]L. Irimpan, V. P. N. Nampoori, P. Radhakrishnan, A. Deepthy, and B. Krishnan, J. Appl. Phys. **102**, 063524(2007).
[63]S. A. M. Lima, F. A. Sigoli, M. Jafelicci, and M. R. Davolos, Int. J. Inorg. Mater. **3**, 749 (2001).
[64]C. V. Manzano, D. Alegre, O. Caballero-Calero, B. Alen, and M. S. Martin-Gonzalez, J. Appl. Phys. **110**, 043538 (2011).